Nanoscale

PAPER

View Article Online
View Journal | View Issue

Cite this: *Nanoscale*, 2022, **14**, 16944

A covalent organic framework/graphene aerogel electrocatalyst for enhanced overall water splitting†

Zhiya Wang,[a] Jingfeng Li,[b] Shiyin Liu,[a] Gaofeng Shao*[c] and Xiaojia Zhao *[a]

Received 10th August 2022,
Accepted 19th October 2022

DOI: 10.1039/d2nr04378e

rsc.li/nanoscale

The rational design of covalent organic framework (COF) based hybrid materials is of paramount importance to address the fundamental challenges of COFs with respect to their poor electron mobilization and the limited number of accessible active sites. Herein, we propose a new strategy for the fabrication of covalently bonded COF grafted graphene aerogel hybrid materials for electrocatalytic application. An *in situ* step-growth polymerization approach was developed to achieve the hybridization of COFs along the surface of amino-functionalized graphene nanosheets. By taking advantage of the three-dimensional conductive networks and highly accessible active sites, the cobalt-incorporated COF/graphene hybrid aerogel shows high oxygen evolution reaction (OER) and hydrogen evolution reaction (HER) performances with an overpotential of 300 and 275 mV at 10 mA cm^{-2}, respectively, under alkaline conditions. When applied to an electrochemical water-splitting electrolyzer, it is able to produce hydrogen and oxygen at competitive rates of 1.14 and 0.58 μL s^{-1}, respectively, under ambient conditions, demonstrating its potential for practical applications.

Introduction

A covalent organic framework (COF) is a new type of crystalline porous polymer that has drawn considerable scientific attention due to its high porosity, adjustable and predictable pore structures, and functional skeletons.[1–6] Particularly, the unique structural characteristics of COFs give them great benefits and possibilities for use in electrocatalytic processes.[7–11] One advantage is that the catalytically active sites can be targeted by predesigning the periodic skeleton, and their tunable electronic structure can offer great opportunities to customize the electrocatalytic performance of COFs.[12] On the other hand, the well-defined pores within COFs provide an unobstructed channel for the diffusion of ions and access to active sites. Thus, the conversion efficiency of energy is substantially improved.[13] For example, Lin and co-workers reported a metalloporphyrin-derived COF with cobalt incorporation for electrocatalytic CO_2 reduction in water.[7] This demonstrated that cobalt centers could have a more delocalized electronic structure due to the interaction between the metal and COF lattices. Consequently, such tunable molecular units within the COF displayed advantageous features of promoting CO_2 reduction to CO with exceptionally high activity and selectivity.

Currently, the research on COF-based electrocatalysts is primarily focused on designing and synthesizing novel COFs at the molecular level.[14–16] Nevertheless, their microporous feature and the absence of any monolithic form largely limit the mass-transport efficiency during heterogeneous catalysis, thus leading to sluggish electrocatalytic activity, especially in a gas-production process.[17–20] Even though our previous research revealed that the introduction of macroporosity in COFs could directly improve their mass transport for water oxidation,[17] the resulting defects within the COFs and the boundaries between particles largely restrict electron transport, making bulk COFs inherently less conductive and limiting their electrocatalytic activities.

Graphene aerogels (GAs), as three-dimensional (3D) conductive networks, have attracted tremendous attention in electrocatalysis field due to their superb electrically conductive and unique mechanical properties.[18,21–24] Very recently, the combination of GAs and COFs has been reported with the aim of improving the conductivity and stability of the COF matrix.[18,25] Notably, the highly accessible area and hierarchical porosity of GAs, on the other hand, are expected to improve

---

[a] *College of Chemistry and Materials Science, Hebei Normal University, Shijiazhuang, 050024, China. E-mail: xiaojia.zhao@hebtu.edu.cn*
[b] *Institute of Microscale Optoelectronics, Shenzhen University, Shenzhen, 518060 P.R. China*
[c] *School of Chemistry and Materials Science, Nanjing University of Information Science & Technology, Nanjing 210044, China. E-mail: gfshao@nuist.edu.cn*

† Electronic supplementary information (ESI) available. See DOI: **https://doi.org/10.1039/d2nr04378e**

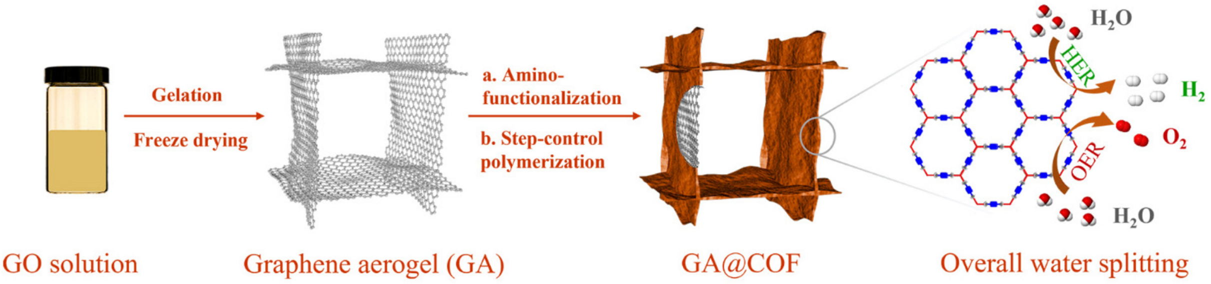

Scheme 1 Schematic representation of GA@COF fabrication.

the efficiency of active sites in COFs and accelerate mass transport. Nevertheless, due to the insoluble nature of COFs and the complicated synthesis thereof, it is technically rather challenging for the *in situ* growth of COFs on GA surfaces through covalent bonds, which could play a critical role in ensuring the synergistic effect described above.

Herein, we have successfully fabricated a hybrid COF/graphene aerogel-based electrocatalyst through the *in situ* growth of COFs on GA surfaces (GA@COF), as schematically illustrated in Scheme 1. Notably, amino-functionalized GA (GA–NH_2) was initially prepared to ensure the covalent bonding of COFs on the graphene surfaces *via* a step-growth polymerization approach. The obtained GA@COF preserves hierarchical pore structures, 3D conductive networks, and stable molecular frameworks, thus resulting in higher electron mobilization and richer accessible active sites. The assessment of enhanced performances was carried out by incorporating Co ions into bipyridine COFs as electrocatalysts, where the obtained Co-coordinated COF coupled with GA (GA@Bpy–COF–Co) exhibits excellent performance as both OER and HER catalysts, demonstrating its potential applications in electrochemical water splitting.

Results and discussion

In a typical synthesis, the graphene aerogel was prepared according to a literature reported procedure (Fig. S1†).[26] To synthesize the amino-functionalized GA, the as-fabricated GA was firstly treated with concentrated hydrochloric acid (HCl) before grafting aminopropyltriethoxysilane (APTES) on its surface.[27] Fourier transform infrared spectroscopy (FTIR) analyses were conducted to confirm the amino functionalities on the GA (GA–NH_2, Fig. S2†). Subsequently, the bipyridine–COF (Bpy–COF) was selected to grow on the GA–NH_2 surfaces by polymerizing the organic linkers 1,3,5 triformylbenzene (TFB) and 2,2′-bipyridine-5,5′-diamine (Bpy) *via* a Schiff base reaction (GA@Bpy–COF, Fig. 1a and Fig. S3†). Notably, a step-growth polymerization approach was applied to ensure the slow polymerization and thus form a uniform distribution of COF layers on graphene surfaces. Specifically, GA–NH_2 was firstly anchored with TFB through a solvothermal method (GA–CHO). Then, the resulting GA–CHO was immersed in 1,4-dioxane with TFB and Bpy additives, followed by uniform growth under ambient conditions for 24 h and subsequent solvothermal treatment at 120 °C for 48 h, respectively, thus forming the hybrid material GA@Bpy–COF (Fig. S4†). As a control, the pristine Bpy–COF was prepared in the absence of the GA following the same process.

Powder X-ray diffraction (PXRD) measurements were applied to characterize the crystallinity of the GA@Bpy–COF, pristine Bpy–COF, and GA. As shown in Fig. 1b, the GA@Bpy–COF shows a strong peak at 3.6° (2θ), which is in agreement with the reflection of the (100) plane in the pristine Bpy–COF, thus supporting the crystalline structure of the COF in the GA@Bpy–COF.[17,28] The broad peak at 24° (2θ) for the GA@Bpy–COF can be attributed to the (002) plane of graphitic carbon from the GA (Fig. S5†).[29] It should be noted that the broad peak at 26° (2θ) for the Bpy–COF originates from the (001) plane corresponding to the π–π stacking of COF layers.

To examine the porosity and specific surface area of the GA@Bpy–COF and Bpy–COF, nitrogen adsorption–desorption isotherms have been recorded. As shown in Fig. 1c, the isotherm of the pristine Bpy–COF exhibits a sharp increase at low relative pressures which indicates the microporous structure of the Bpy–COF. The result was corroborated further by examining the corresponding pore size distribution (Fig. S6†). In contrast, the GA@Bpy–COF exhibits a typical type IV isotherm, with a hysteretic loop clearly visible at higher relative pressures, which indicates the existence of meso- and macroporosity derived from the GA networks. Besides, the Brunnauer–Emmett–Teller (BET) surface areas were calculated indicating that the GA@Bpy–COF (412 $m^2\ g^{-1}$) has a much higher surface area than the pristine GA (34 $m^2\ g^{-1}$) demonstrating the formation of the hybrid material GA@Bpy–COF.

The morphological features of the GA and GA@Bpy–COF have been characterized by scanning electron microscopy (SEM) analyses. As shown in Fig. 1d and e, a sponge-like structure, consisting of extended and inter-linked graphene nanosheets, was observed, demonstrating the successful formation of the GA. Typically, the formed GA is recognized to have pore sizes in the micrometer range along with macroporous channels to facilitate efficient mass transfer (Fig. S7†). Similarly, the morphological structure of the GA@Bpy–COF has no obvious changes with 3D interconnected networks while the roughness of the graphene surfaces proves the

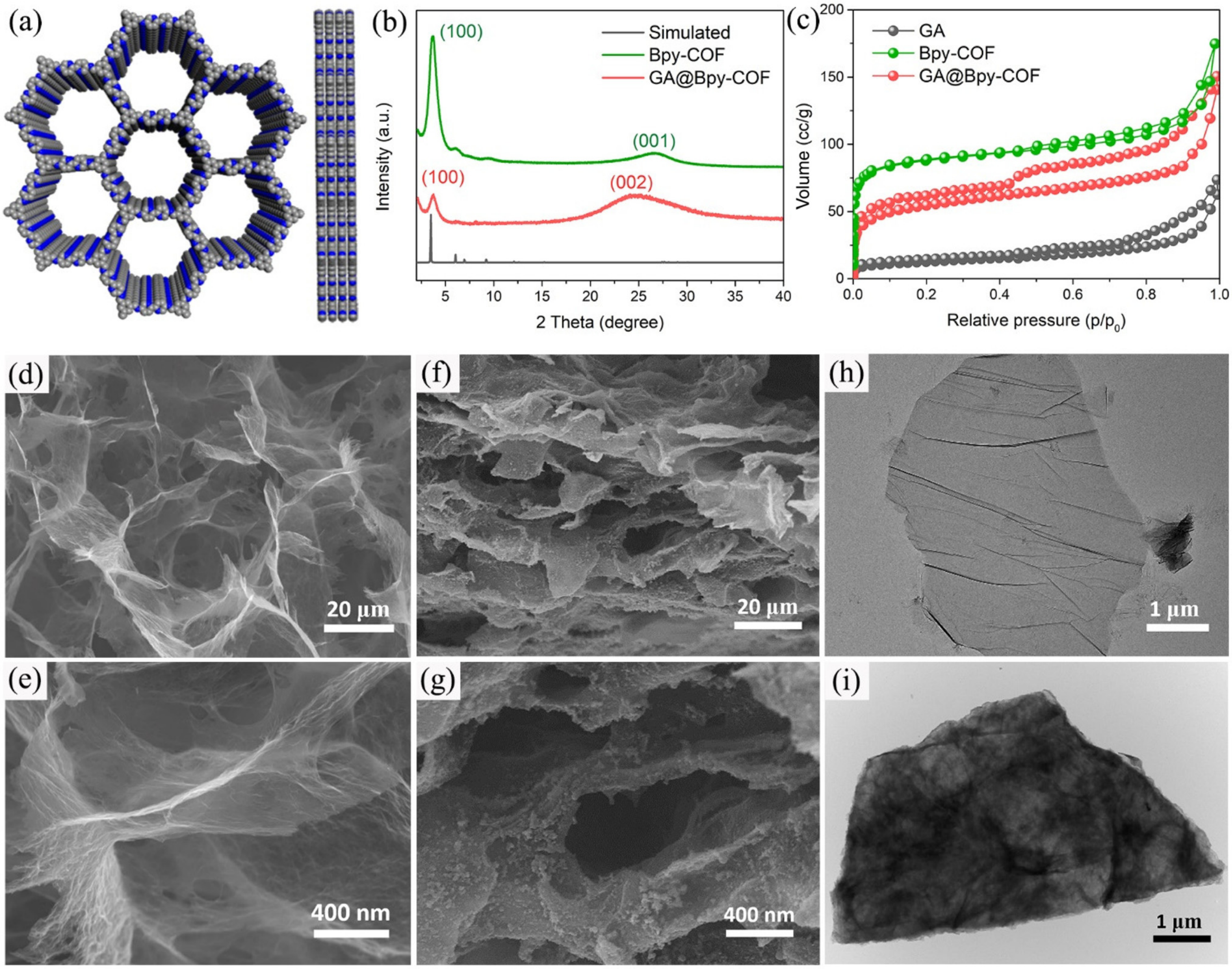

Fig. 1 (a) Space-filling packing diagram of Bpy–COF from different views. (b) PXRD patterns of the pristine Bpy–COF and GA@Bpy–COF. (c) N_2 sorption isotherms of the GA, Bpy–COF and GA@Bpy–COF. (d and e) SEM images of the GA. (f and g) SEM images of the GA@Bpy–COF. TEM images of (h) graphene and (i) the GA@Bpy–COF.

growth of COFs on the GA (Fig. 1f and g and Fig. S8†). Transmission electron microscopy (TEM) was conducted to further demonstrate that no isolated COF particles were detected on the graphene nanosheets, suggesting the uniform growth of COFs across the surface of graphene (Fig. 1h and i and Fig. S9†). Comparatively, the GA without amino functionalities was applied as the substrate for COF growth. The bulk and aggregated COF particles on the graphene surface demonstrate the critical role of the amino group in the formation of covalently bonded COF grafted GA hybrid materials (Fig. S10†).

Transition metal-based electrocatalysts are currently being investigated widely as promising electrocatalysts.[30–35] In this study, a bipyridine amine linker (Bpy) was deliberately selected due to its ability to strongly coordinate with metal ions, mimicking the molecular systems of metal and bipyridine.[36,37] Accordingly, cobalt ions have been preferentially used to construct GA@Bpy–COF–Co by soaking the GA@Bpy–COF in Co$(OAc)_2·4H_2O$ methanol solutions and further stirring for 4 h under ambient conditions (Fig. 2a).[17] For comparison, the pristine Bpy–COF was used in the preparation of Bpy–COF–Co by following the same protocol.

Typically, the PXRD pattern shows the preservation of crystallinity after cobalt coordination in GA@Bpy–COF–Co (Fig. S11†). X-ray photoelectron spectroscopy (XPS) confirms the existence of Co species in GA@Bpy–COF–Co and Bpy–COF–Co, giving an amount of 2.34 and 2.66 atomic %, respectively (Fig. S12a†). The accurate loadings of Co were quantified by inductively coupled plasma-optical emission spectrometry (ICP-OES), corresponding to 8.157 wt% and 8.232 wt%, respectively. Specifically, the Co 2p XPS spectra show two main peaks centered at 780 and 796 eV, corresponding to the Co $2p_{3/2}$ and Co $2p_{1/2}$ core levels, respectively, while the appearance of a satellite peak at 785 eV is attributed to the existence of Co^{2+} (Fig. 2b).[38] Notably, an extra peak (399.6 eV) was observed in the high-resolution N 1s spectra of GA@Bpy–COF–

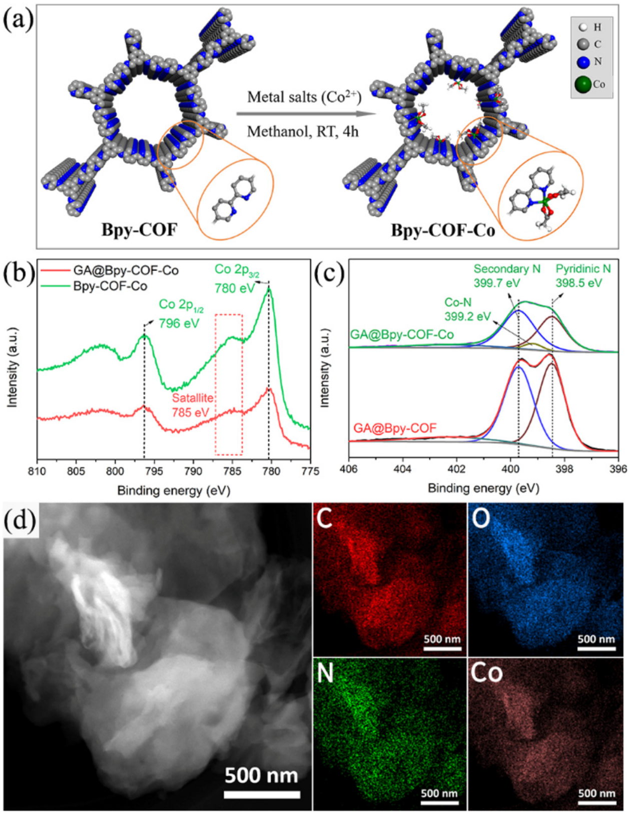

Fig. 2 (a) Schematic illustration of the fabrication of GA@Bpy–COF–Co. (b) Co 2p XPS spectra of GA@Bpy–COF–Co and Bpy–COF–Co. (c) N 1s XPS spectra of GA@Bpy–COF–Co and the GA@Bpy–COF. (d) HAADF-STEM images with the corresponding elemental mappings of C, O, N, and Co.

Co compared to the GA@Bpy–COF, and is assigned to the Co–N bond, indicating the coordination between Co ions and pyridine N within the COF backbone (Fig. 2c).[31] As well, a similar spectrum confirms the presence of the Co–N bond in Bpy–COF–Co (Fig. S12b†). To demonstrate the element distribution in GA@Bpy–COF–Co, high-angle annular dark-field scanning transmission electron microscopy (HAADF-STEM) was conducted, revealing the uniform distribution of C, O, N, and Co elements throughout the matrix of GA@Bpy–COF–Co (Fig. 2d).

To verify the critical role of the graphene aerogel in electrocatalytic applications, a three-electrode system has been initially used to evaluate the OER activity of GA@Bpy–COF–Co under alkaline conditions (0.1 M KOH). For comparison, the electrocatalytic activities of Bpy–COF–Co, GA@Bpy–COF and RuO_2 with the same mass loadings of 0.25 mg cm^{-2} were studied. Fig. 3a shows that GA@Bpy–COF–Co exhibits the lowest overpotential of 300 mV (*vs.* the RHE, reversible hydrogen electrode) at a current density of 10 mA cm^{-2} (Fig. S13a†), compared to those of Bpy–COF–Co (350 mV), GA@Bpy–COF (660 mV), RuO_2 (330 mV) and some other similarly characterized Co-based OER catalysts (Table S1†). In the corresponding Tafel slope, GA@Bpy–COF–Co shows a lower linear slope of 54 mV dec^{-1} than Bpy–COF–Co (85 mV dec^{-1}), GA@Bpy–COF (259 mV dec^{-1}) and RuO_2 (89 mV dec^{-1}), demonstrating its superior reaction kinetics during the OER process (Fig. 3b). Notably, the enhanced performance of GA@Bpy–COF–Co over Bpy–COF–Co could be explained by the interconnected graphene networks, which remarkably facilitate the electron transport and increase the active site efficiency under the OER process. The superior electron transfer kinetics is further demonstrated by electrochemical impedance spectroscopy (EIS), where the smaller semicircle in the Nyquist plot of GA@Bpy–COF–Co indicates an apparent decrease of interfacial charge transfer resistance (R_{ct}), which subsequently induces the facilitated charge transfer to promote the OER activity (Fig. S14a†). In addition, to validate Co ions that are responsible for the OER activity of GA@Bpy–COF–Co, the effect of thiocyanate ions (SCN^-), which could strongly bind to cobalt sites, on the performance of GA@Bpy–COF–Co was examined.[17,39] As shown in Fig. 3c, the overpotential of GA@Bpy–COF–Co at 10 mA cm^{-2} increased substantially when SCN^- was added (10 mM) to the electrolyte, demonstrating the critical role of Co sites in the OER process. The oxidation states of Co were studied by cyclic voltammetry (CV), where the redox peaks can be well identified in GA@Bpy–COF–Co and Bpy–COF–Co, demonstrating the quasi-reversible Co^{2+}/Co^{3+} couple during the OER (Fig. S15†). Furthermore, the turnover frequency (TOF), indicating the intrinsic catalytic activity of a catalyst at an atomic level, has been calculated to build a plot of TOF values against the applied potential (Fig. S16†). It can be observed that GA@Bpy–COF–Co exhibits a higher TOF value than Bpy–COF–Co during the OER.

Inspired by the promising OER performance of GA@Bpy–COF–Co, the hydrogen evolution reaction (HER) has been studied under the same alkaline conditions (0.1 M KOH). For comparison, a commercial catalyst with a 20 wt% Pt/C mass loading of 0.25 mg cm^{-2} was tested. As shown in Fig. 3d, GA@Bpy–COF–Co exhibits a comparable overpotential of 275 mV at a current density of 10 mA cm^{-2} (Fig. S13b†), which is significantly lower than those of Bpy–COF–Co (440 mV) and GA@Bpy–COF (710 mV) and some other reported Co-based HER catalysts (Table S1†). The corresponding Tafel slopes and Nyquist plots further confirm that GA@Bpy–COF–Co exhibits higher reaction kinetics and displays an enhanced electron transfer pathway in the HER process (Fig. 3e and Fig. S14b†). In tests of stability and durability of catalysts, GA@Bpy–COF–Co shows no significant differences in the required overpotential at a current density of 10 mA cm^{-2} for both the OER and HER (Fig. S17†). In addition, the chronopotentiometry response of GA@Bpy–COF–Co upon the addition of SCN^- demonstrated the role of Co ions as active sites in the HER catalytic process (Fig. 3f). To better understand the intrinsic electrocatalytic activity, the electrochemical surface areas (ECSA) of Bpy–COF–Co and GA@Bpy–COF–Co were initially estimated by measuring the capacitance of the double layer (C_{dl}) at the solid–liquid interface using CV (Fig. S18a and b†). As shown in Fig. S18c,† the C_{dl} value of GA@Bpy–COF–Co is higher than that of Bpy–COF–Co, demonstrating the higher ECSA of GA@Bpy–COF–Co. In addition, the LSV curves were

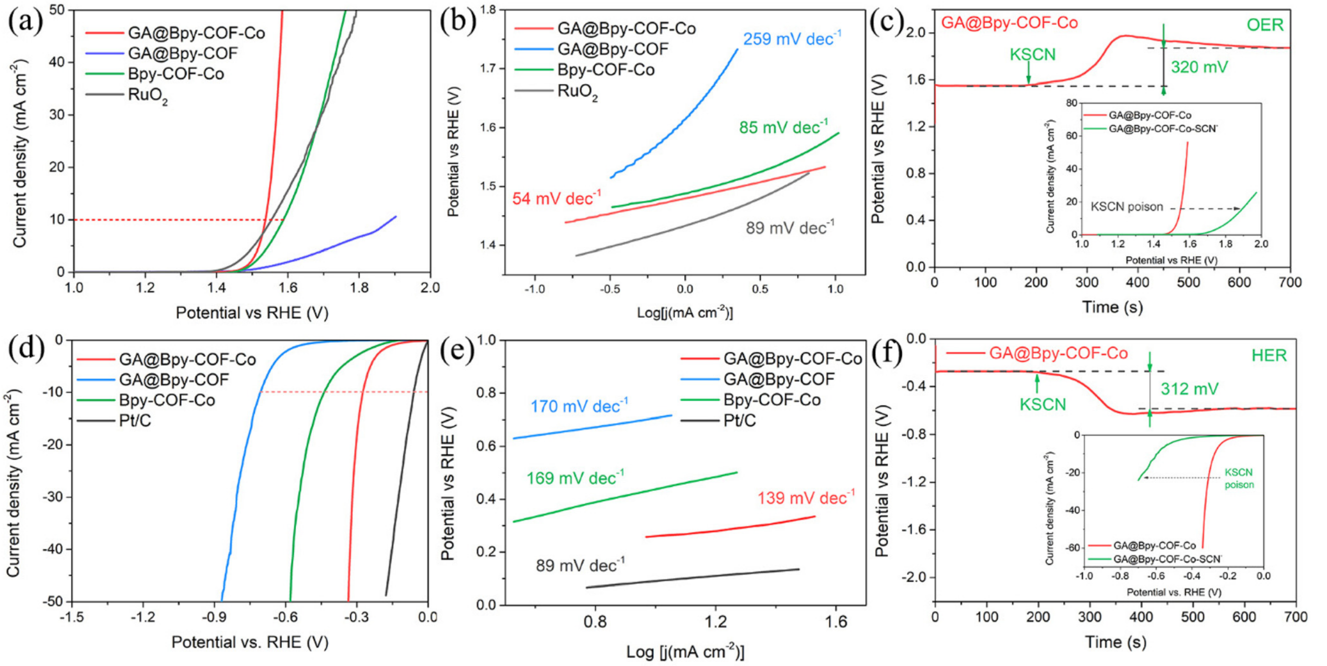

Fig. 3 (a) OER polarization curves and (b) corresponding Tafel plots for GA@Bpy–COF–Co, GA@Bpy–COF, Bpy–COF–Co, and the RuO_2 catalyst. (c) Chronopotentiometry response of GA@Bpy–COF–Co upon addition of 10 mM SCN^- into the electrolyte after 200 s. Inset: polarization plots of GA@Bpy–COF–Co before and after the addition of 10 mM SCN^- in the OER process. (d) HER polarization curves and (e) corresponding Tafel plots for GA@Bpy–COF–Co, GA@Bpy–COF, Bpy–COF–Co, and the Pt/C catalyst. (f) Chronopotentiometry response of GA@Bpy–COF–Co upon addition of 10 mM SCN^- into the electrolyte after 200 s. Inset: polarization plots of GA@Bpy–COF–Co before and after the addition of 10 mM SCN^- in the HER process.

normalized by the ECSA to determine the intrinsic HER and OER activities (Fig. S18d and e†). Similar to that of current density normalized by the geometric surface area, GA@Bpy–COF–Co shows higher ECSA-normalized current density than Bpy–COF–Co for both the HER and OER at a given potential, indicating its superior intrinsic electrocatalytic activities. To verify the importance of the amino group on the GA surface, the HER and OER activities of GA@Bpy–COF–Co-non were studied (Fig. S19†), where the superior performances of GA@Bpy–COF–Co can be attributed to the uniform distribution of COFs on the GA surface which is consistent with the observation of TEM analysis. Furthermore, the critical role of the crystalline structure of the COF in catalytic activity has been proved by comparing the HER and OER performances of Bpy–COF–Co and Bpy–Co (Fig. S20†). For comparison, other transition metal ions were tested instead of Co^{2+} by performing both the OER and HER under the same conditions, including nickel (Ni^{2+}), iron (Fe^{2+}), zinc (Zn^{2+}), copper (Cu^{2+}), and manganese (Mn^{2+}). As a result, all the GA@Bpy–COF–M compounds with other metal species exhibit lower electrocatalytic activities for both the OER and HER (Fig. S21†).

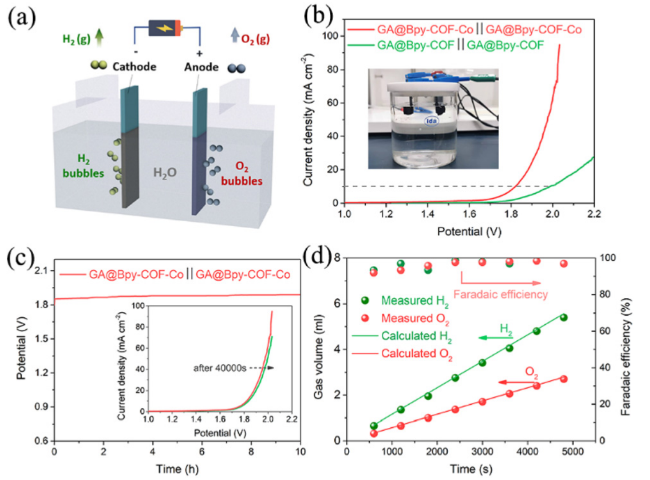

Fig. 4 (a) Schematic diagram of an electrolyzer for water splitting. (b) Polarization curve of GA@Bpy–COF–Co‖GA@Bpy–COF–Co and the GA@Bpy–COF‖GA@Bpy–COF. Inset: photograph of the two-electrode configuration. (c) Chronopotentiometry test for GA@Bpy–COF–Co at a constant current density of 10 mA cm^{-2}. Inset: polarization curves before and after 40 000 s of durability test. (d) The gas volumes of H_2 and O_2 and corresponding faradaic efficiency as a function of water splitting time for GA@Bpy–COF–Co.

Based on the above studies, it is clearly demonstrated that GA@Bpy–COF–Co is a promising bifunctional electrocatalyst for both the OER and HER. As such, we constructed an electrolyzer with GA@Bpy–COF–Co as both the cathode and anode to split water at room temperature (Fig. 4a). In order to get fully connected with these GA-based electrodes, graphitic nanorods (D = 2 mm) were applied to insert into the GA during its fabrication process (Fig. S22†). Fig. 4b shows the linear sweep voltammetry (LSV) curves of water electrolysis on the GA@Bpy–COF–Co‖GA@Bpy–COF–Co electrodes in 1.0 M KOH solution.

For comparison, the GA@Bpy–COF||GA@Bpy–COF was tested with the same volume of reactive area. During overall water splitting, GA@Bpy–COF–Co possesses a comparable cell voltage of 1.82 V to the GA@Bpy–COF (1.98 V) at a current density of 10 mA cm^{-2} (Fig. 4b). The chronopotentiometry test was performed at a current density of 10 mA cm^{-2} to demonstrate the high stability of GA@Bpy–COF–Co after 10 hours of operation (Fig. 4c). Furthermore, gas volumes of H_2 and O_2 were recorded as functions of water-splitting time at a current density of 10 mA cm^{-2}, where a linear relationship was built with a slope of 1.14 and 0.58 μL s^{-1} for H_2 and O_2 production, respectively (Fig. S23 and Table S2†). Accordingly, the agreement between the experimentally generated quantities of H_2 and O_2 and the theoretical calculations demonstrated that the faradaic efficiency for the HER and OER in KOH is approximately 100% (Fig. 4d).

Chemical stability is of importance for catalysts to value their practical application in electrocatalytic processes. Considering the applied high-potential at the anode electrode, the structural feature of GA@Bpy–COF–Co after 10 h of OER testing was typically investigated using SEM analysis. As shown in Fig. 5a, the morphology and 3D interconnected networks of GA@Bpy–COF–Co-10 h are preserved. Meanwhile, the roughness of graphene surfaces shows the conservation of COFs on the GA (Fig. 5b), which was further proved by the PXRD pattern that the crystalline structure of COFs is well-maintained after the long-term reaction under alkaline conditions (Fig. 5c). Furthermore, the TEM image of GA@Bpy–COF–Co-10 h shows that no isolated metal particles or COF particles were detected on the graphene surfaces (Fig. S24†). Co 2p XPS spectra were recorded to analyze the valence changes of active centers in GA@Bpy–COF–Co-10 h. As shown in Fig. 5(d), the binding energy at the Co 2p level exhibits no distinct changes compared to that of GA@Bpy–COF–Co. The disappearance of the satellite peak (785 eV) at Co 2p in GA@Bpy–COF–Co-10 h indicates the presence of oxidation states (CO^{2+} and Co^{3+}) after the OER, which is consistent with the previous report.[17]

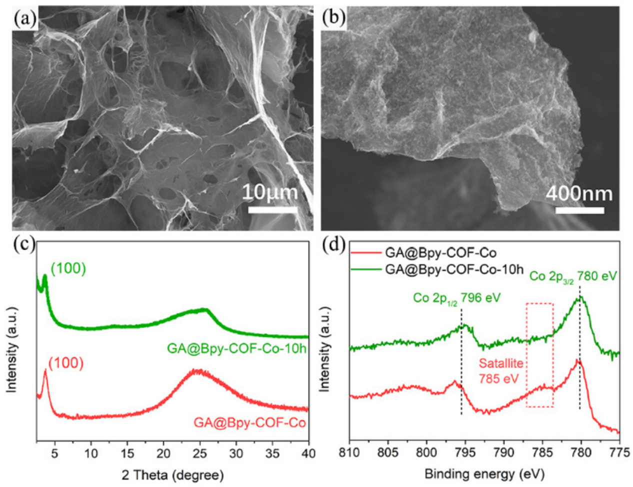

Fig. 5 (a and b) SEM images of GA@Bpy–COF–Co after 10 h of OER testing. (c) PXRD pattern and (d) Co 2p spectra of GA@Bpy–COF–Co before and after 10 h of OER testing.

Conclusions

In conclusion, we proposed an *in situ* step-growth polymerization strategy to fabricate covalently bonded COF grafted graphene aerogel hybrid materials as efficient electrocatalysts. The as-fabricated composite aerogel featuring a hierarchical pore structure and highly accessible surface areas can achieve the rapid mass transport capacity of ions/electrons and can be favorable for the efficient utilization of abundant accessible redox active sites. Due to the *in situ* growth of the bipyridine COF on the graphene networks, the fabricated GA@Bpy–COF–Co exhibits impressive catalytic activity for both the OER and HER under alkaline conditions, thus showing practical applications in overall water splitting. This study provides a novel strategy for the processing of hybrid COF materials and paves the way for the practical application of COF-based electrocatalysts in the future.

Author contributions

Z. Y. Wang and J. F. Li contributed equally to this work. Z. Y. Wang performed the experiments and developed the method. J. F. Li conducted most of the characterization studies of the samples. S. Y. Liu prepared and reproduced some of the samples. G. F. Shao helped in organizing and writing the manuscript. X. J. Zhao directed the project and wrote the manuscript with the feedback from other authors.

Conflicts of interest

There are no conflicts to declare.

Acknowledgements

This work was supported by the Natural Science Foundation of Hebei Province (E2020205004) and the National Natural Science Foundation of China (22105060). The funding by the National Natural Science Foundation of China (52102361) is acknowledged.

References

1 A. Cote, A. Benin, N. Ockwig, M. O'Keeffe, A. Matzger and O. Yaghi, Porous, crystalline, covalent organic frameworks, *Science*, 2005, **310**, 1166–1170.

2 N. Huang, P. Wang and D. Jiang, Covalent organic frameworks: a materials platform for structural and functional designs, *Nat. Rev. Mater.*, 2016, **1**, 16068.

3 D. Jiang, Covalent organic frameworks: chemical approaches to designer structures and built-in functions, *Angew. Chem., Int. Ed.*, 2019, **59**, 5050–5091.

4 C. Diercks and O. Yaghi, The atom, the molecule, and the covalent organic framework, *Science*, 2017, **355**, 1585.

5 R. Liu, K. Tan, Y. Gong, Y. Chen, Z. Li, S. Xie, T. He, Z. Lu, H. Yang and D. Jiang, Covalent organic frameworks: an ideal platform for designing ordered materials and advanced applications, *Chem. Soc. Rev.*, 2021, **50**, 120–242.

6 A. Evans, M. Strauss, A. Corcos, Z. Hirani, W. Ji, L. Hamachi, X. Aguilar-Enriquez, A. Chavez, B. Smith and W. Dichtel, Two-dimensional polymers and polymerizations, *Chem. Rev.*, 2022, **122**, 442–564.

7 S. Lin, C. Diercks, Y. Zhang, N. Kornienko, E. Nichols, Y. Zhao, A. Paris, D. Kim, P. Yang, O. Yaghi and C. Chang, Covalent organic frameworks comprising cobalt porphyrins for catalytic CO_2 reduction in water, *Science*, 2015, **49**, 1208–1213.

8 A. Halder, M. Ghosh, M. Khayum, S. Bera, M. Addicoat, H. Sasmal, S. Karak, S. Kurungot and R. Banerjee, Interlayer hydrogen-bonded covalent organic frameworks as high-performance supercapacitors, *J. Am. Chem. Soc.*, 2018, **140**, 10941–10945.

9 J. Li, X. Jing, Q. Li, S. Li, X. Gao, X. Feng and B. Wang, Bulk COFs and COF nanosheets for electrochemical energy storage and conversion, *Chem. Soc. Rev.*, 2020, **49**, 3565–3604.

10 X. Zhao, P. Pachfule and A. Thomas, Covalent organic frameworks (COFs) for electrochemical applications, *Chem. Soc. Rev.*, 2021, **50**, 6871–6913.

11 H. Aiyappa, J. Thote, D. Shinde, R. Banerjee and S. Kurungot, Cobalt-modified covalent organic framework as a robust water oxidation electrocatalyst, *Chem. Mater.*, 2016, **28**, 4375–4379.

12 T. Li, X. Yan, W. Zhang, W. Han, Y. Liu, Y. Li, H. Zhu, Z. Li and Z. Gu, A 2D donor–acceptor covalent organic framework with charge transfer for supercapacitors, *Chem. Commun.*, 2020, **56**, 14187–14190.

13 Y. Lu, Y. Cai, Q. Zhang and J. Chen, Structure–performance relationships of covalent organic framework electrode materials in metal-ion batteries, *J. Phys. Chem. Lett.*, 2021, **12**, 8061–8071.

14 H. Xu, J. Gao and D. Jiang, Stable, crystalline, porous, covalent organic frameworks as a platform for chiral organocatalysts, *Nat. Chem.*, 2015, **7**, 905–912.

15 Q. Zhu, X. Wang, R. Clowes, P. Cui, L. Chen, M. Little and A. Cooper, 3D cage COFs: a dynamic three-dimensional covalent organic framework with high-connectivity organic cage nodes, *J. Am. Chem. Soc.*, 2020, **142**, 16842–16848.

16 Y. Li, W. Chen, G. Xing, D. Jiang and L. Chen, New synthetic strategies toward covalent organic frameworks, *Chem. Soc. Rev.*, 2020, **49**, 2852–2868.

17 X. Zhao, P. Pachfule, S. Li, T. Langenhahn, M. Ye, C. Schlesiger, S. Praetz, J. Schmidt and A. Thomas, Macro/microporous covalent organic frameworks for efficient electrocatalysis, *J. Am. Chem. Soc.*, 2019, **141**, 6623–6630.

18 C. Li, J. Yang, P. Pachfule, S. Li, M. Ye and J. Schmidt, Ultralight covalent organic framework/graphene aerogels with hierarchical porosity, *Nat. Commun.*, 2020, **11**, 4712.

19 F. Haase, P. Hirschle, R. Freund, S. Furukawa, Z. Ji and S. Wuttke, Beyond frameworks: structuring reticular materials across nano-, meso-, and bulk regimes, *Angew. Chem., Int. Ed.*, 2020, **59**, 22350–22370.

20 S. Kandambeth, K. Dey and R. Banerjee, Covalent organic frameworks: chemistry beyond the structure, *J. Am. Chem. Soc.*, 2019, **141**, 1807–1822.

21 L. Qiu, J. Liu, S. Chang, Y. Wu and D. Li, Biomimetic superelastic graphene-based cellular monoliths, *Nat. Commun.*, 2012, **3**, 1241.

22 X. Zhang, Z. Sui, B. Xu, S. Yue, Y. Luo, W. Zhan and B. Liu, Mechanically strong and highly conductive graphene aerogel and its use as electrodes for electrochemical power sources, *J. Mater. Chem.*, 2011, **21**, 6494–6497.

23 H. Yang, Z. Li, B. Lu, J. Gao, X. Jin, G. Sun, G. Zhang, P. Zhang and L. Qu, Reconstruction of inherent graphene oxide liquid crystals for large-scale fabrication of structure-intact graphene aerogel bulk toward practical applications, *ACS Nano*, 2018, **12**, 11407–11416.

24 M. Seredych, K. László, E. Rodríguez-Castellón and T. Bandosz, S-doped carbon aerogels/GO composites as oxygen reduction catalysts, *J. Energy Chem.*, 2016, **25**, 236–245.

25 C. Li, S. Cao, J. Lutzki, J. Yang, T. Konegger, F. Kleitz and A. Thomas, A covalent organic framework/graphene dual-region hydrogel for enhanced solar-driven water generation, *J. Am. Chem. Soc.*, 2022, **144**, 3083–3090.

26 X. Huang, G. Yu, Y. Zhang, M. Zhang and G. Shao, Design of cellular structure of graphene aerogels for electromagnetic wave absorption, *Chem. Eng. J.*, 2021, **426**, 131894.

27 Y. Lin, J. Jin and M. Song, Preparation and characterisation of covalent polymer functionalized graphene oxide, *J. Mater. Chem.*, 2011, **21**, 3455–3461.

28 X. Zhao, P. Pachfule, S. Li, T. Langenhahn, M. Ye, G. Tian, J. Schmidt and A. Thomas, Silica-templated covalent organic framework-derived Fe–N-doped mesoporous carbon as oxygen reduction electrocatalyst, *Chem. Mater.*, 2019, **31**, 3274–3280.

29 N. An, Z. Guo, J. Xin, Y. He, K. Xie, D. Sun, X. Dong and Z. Hu, Hierarchical porous covalent organic framework/graphene aerogel electrode for high-performance supercapacitors, *J. Mater. Chem. A*, 2021, **9**, 16824–16833.

30 X. Zhao, P. Pachfule, S. Li, J. Simke, J. Schmidt and A. Thomas, Bifunctional electrocatalysts for overall water splitting from an Iron/Nickel-based bimetallic metal–organic framework/dicyandiamide composite, *Angew. Chem., Int. Ed.*, 2018, **57**, 8921–8926.

31 C. Cheng, S. Li, Y. Xia, L. Ma, C. Nie, C. Roth, A. Thomas and R. Haag, Atomic Fe–Nx coupled open-mesoporous carbon nanofibers for efficient and bioadaptable oxygen electrode in Mg–air batteries, *Adv. Mater.*, 2018, **30**, 1802669.

32 F. Song, L. Bai, A. Moysiadou, S. Lee, C. Hu, L. Liardet and X. Hu, Transition Metal Oxides as Electrocatalysts for the

Oxygen Evolution Reaction in Alkaline Solutions: An Application-Inspired Renaissance, *J. Am. Chem. Soc.*, 2018, **140**, 7748–7759.

33 H. Sun, Z. Yan, F. Liu, W. Xu, F. Cheng and J. Chen, Self-supported transition-metal-based electrocatalysts for hydrogen and oxygen evolution, *Adv. Mater.*, 2020, **32**, 1806326.

34 D. Li, S. Liu, G. Ye, W. Zhu, K. Zhao, M. Luo and Z. He, One-step electrodeposition of NixFe3−xO4/Ni hybrid nanosheet arrays as highly active and robust electrocatalysts for the oxygen evolution reaction, *Green Chem.*, 2020, **22**, 1710–1719.

35 L. Chen, J.-T. Ren and Z.-Y. Yuan, Design strategies of phosphorus-containing catalysts for photocatalytic, photoelectrochemical and electrocatalytic water splitting, *Green Chem.*, 2022, **24**, 713–747.

36 P. Zhang, X. Yang, X. Hou, X. Xu, B. Xiao, J. Huang and C. Stampfl, Metal–bipyridine complexes as electrocatalysts for the reduction of CO2: a density functional theory study, *Phys. Chem. Chem. Phys.*, 2019, **21**, 23742–23748.

37 S. Hooe, A. Rheingold and C. Machan, Electrocatalytic reduction of dioxygen to hydrogen peroxide by a molecular manganese complex with a bipyridine-containing schiff base ligand, *J. Am. Chem. Soc.*, 2018, **140**, 3232–3241.

38 M. Biesinger, B. Payne, A. Grosvenor, L. Lau, A. Gerson and R. Smart, Resolving surface chemical states in XPS analysis of first row transition metals, oxides and hydroxides: Cr, Mn, Fe, Co and Ni, *Appl. Surf. Sci.*, 2011, **257**, 2717–2730.

39 S. Dou, C. Dong, Z. Hu, Y. Huang, J. Chen, L. Tao, D. Yan, D. Chen, S. Shen, S. Chou and S. Wang, Atomic-scale CoOx species in metal–organic frameworks for oxygen evolution reaction, *Adv. Funct. Mater.*, 2017, **27**, 1702546.